Supplementary material to the paper: "*Evidence arguing against the validity of the no-slip boundary condition: blood flow in vivo*"

This supplement provides details of the overall approach used in determining the effect of slippage and the inlet velocity in the unsteady flow simulations governed by Navier-Stokes equations, coupled with four-dimensional magnetic resonance imaging (4D MRI). As suggested in [21], it is not necessary to incorporate turbulence effects in considered pulsatile flows. There are numerous studies investigating occurence of slip in specific situations see for example [22, 5, 18] and references cited in [11, 12]. The method was developed initially in [8], where, however, the underlying system of partial differential equations (PDEs) consists of stationary (time-independent) Navier-Stokes equations. There are also other differences between this study and [8]; we state them below when explaining some specific issues.

The scheme of this supplement is the following. In Section 1, we give a complete mathematical description of the overall mathematical problem at a continuous (infinite-dimensional) level; it belongs to the class of PDE-constrained optimization problems. Then, in Section 2, the details regarding segmentation and MRI data preparation are given. Section 3 concerns finite-dimensional (finite-element) approximations and relevant issues. Finally, in Section 4, we summarize all types of tests performed, which support our principal findings. Toward this goal, we work not only on real patient-specific geometries (descending thoraric aorta), but also on artificial designed geometrical domains.

1 Methodology

Our core initial and boundary value PDE problem consists in finding the solution of the incompressible Navier-Stokes in three-dimensional tube-like domains with the apparently given velocity at the inlet, and the slip parameter at the wall. We determine these parameters by integrating available 4D MRI data into the overall model, requiring that the solution of the PDE problem corresponding to these values is the best approximation of the data. In what follows, we describe first the governing PDE problem and then we consider it within the context of optimization/data assimilation framework.

1.1 Governing PDE problem

We consider unsteady flow of fluid (blood) in a three-dimensional domain Ω, representing a part of the aorta; see Figure 4 for real patient-specific domains (see also Section 2 for details) or Figure 1 for artificially designed domains that mimic parts of aorta. In all cases, the boundary $\partial\Omega$ consists of three parts: the inlet Γ_{in}, the outlet Γ_{out}, and the vessel wall surface Γ_{wall}, each associated with distinct boundary conditions in the model. While the inlet and outlet are artificial boundaries introduced to define the domain of interest, Γ_{wall} represents the interface between the flow domain and the vessel wall.

Inside the flow domain Ω, we assume that the blood flow in the aorta is well described by the incompressible Navier-Stokes equations, characterized by the velocity field $\mathbf{v}$ and the mean normal stress (the pressure) p. These equations include two positive parameters, the density ρ and the dynamic viscosity μ. In this study, these values are assumed to be constant, and correspond to standard values for human blood.

On Γ_{wall}, we impose an impermeability condition (i.e., no flow in the normal direction) while allowing the fluid to slip along the wall in the tangential directions. The extent of this slip ranges from perfect slip (a frictionless wall), through Navier's slip condition (where the tangential velocity is proportional to the projection of the traction onto the tangent plane), to no-slip (where the fluid adheres completely to the boundary). All these scenarios are captured by the slip parameter κ, which represents the degree of friction: $\kappa = 0$ corresponds to a frictionless surface (full slip), while $\kappa = +\infty$ corresponds to the situation where the fluid does not slip (no slip). At the inlet, it would be desirable to prescribe $\mathbf{v}_{\mathrm{in}}$ for the velocity field. At the outlet, assuming that it is chosen appropriately, we assume that the flow occurs only in the normal direction with respect to the cross-section. Alternatively, one could consider the free-flow condition at the outlet; this condition is however not satisfied by unidirectional Poiseuille flow, while the condition considered in this study does not have this deficiency.

With all this in mind, the system of governing equations takes the following form:

$$
\begin{aligned}
\rho\,\partial_t \mathbf{v} + \rho(\nabla\mathbf{v})\mathbf{v} - \operatorname{div}\mathbb{T}(\mathbf{v},p) &= \mathbf{0} && \text{in } (0,T)\times\Omega,\\
\mathbb{T}(\mathbf{v},p) &= -p\,\mathbb{I} + 2\mu\mathbb{D}(\mathbf{v}) && \text{in } (0,T)\times\Omega,\\
\operatorname{div}\mathbf{v} &= 0 && \text{in } (0,T)\times\Omega,\\
\mathbf{v}(0,\cdot) &= \mathbf{v}_0 && \text{in } \Omega,\\
\mathbf{v} &= \mathbf{v}_{\mathrm{in}} && \text{on } (0,T)\times\Gamma_{\mathrm{in}},\\
(\mathbb{T}(\mathbf{v},p)\,\mathbf{n})\cdot\mathbf{n} = \frac{1}{2}\,\rho\,(\mathbf{v}\cdot\mathbf{n})_-^2 \quad \text{and} \quad \mathbf{v}_\tau &= \mathbf{0} && \text{on } (0,T)\times\Gamma_{\mathrm{out}},\\
\kappa\,\mathbf{v}_\tau = -(\mathbb{T}(\mathbf{v},p)\,\mathbf{n})_\tau \quad \text{and} \quad \mathbf{v}\cdot\mathbf{n} &= 0 && \text{on } (0,T)\times\Gamma_{\mathrm{wall}}.
\end{aligned}
\tag{1}
$$

Here, $T > 0$ is the terminal time of the period of our interest, $\mathbb{T}$ denotes the Cauchy stress tensor, which appears in the balance of linear momentum (the first equation), the constitutive relation for an incompressible Navier–Stokes fluid (the second equation), the directional free outflow condition at the outlet (the first identity in the next-to-last line), and the Navier slip boundary condition (the first identity in the last line). The third equation represents the incompressibility constraint. Furthermore, $\mathbf{v}_0$, which appears in the fourth equation, denotes the initial condition for the velocity field; in all numerical tests conducted in this study, is set to zero.

In reality, specifying the inlet velocity $\mathbf{v}_{\mathrm{in}}$ and the wall slip parameter κ is not feasible. Therefore, we treat them as unknowns, and determine their values based on the available 4D MRI data through an assimilation process, as developed in [8] and briefly described in the next section. This approach allows us to treat these parameters as spatially varying.

Importantly, the slip parameter κ must be non-negative due to the physical requirement that the total dissipation resulting from fluid–wall interaction must be non-negative, in accordance with the Second Law of Thermodynamics. However, the constraint $\kappa > 0$ introduces certain limitations—such as the inapplicability of some numerical methods and computational tools. To address this, we introduce an auxiliary slip parameter K, which is allowed to take any real value in the range $(-\infty, +\infty)$, and relate it to κ via the transformation:

$$
K = \ln\kappa \qquad \Longleftrightarrow \qquad \kappa = \exp K. \tag{2}
$$

1.2 Data assimilation - PDE constrained optimization

To measure the difference between the given velocity data $\mathbf{d}_{\mathrm{MRI}}$ (generated either artifically or obtained from 4D MRI of real patients) and the velocity field $\mathbf{v} = \mathbf{v}(\mathbf{v}_{\mathrm{in}}, K)$ obtained by the solution of (1) and viewed as the function of $\mathbf{v}_{\mathrm{in}}$ and K that we wish to determine, we introduce the functional $\mathcal{J}$ as the L^2 norm of their difference, i.e.,

$$\mathcal{J}(\mathbf{v}(\mathbf{v}_{\mathrm{in}}, K)) = \frac{1}{2}\|\mathcal{T}(\mathbf{v}(\mathbf{v}_{\mathrm{in}}, K)) - \mathbf{d}_{\mathrm{MRI}}\|^2_{L^2(0,T,L^2(\Omega))} := \int_0^T \int_\Omega |\mathcal{T}(\mathbf{v}) - \mathbf{d}_{\mathrm{MRI}}|^2 \,\mathrm{d}x\mathrm{d}t, \tag{3}$$

where $\mathcal{T}$ is the measurement operator that maps the velocity field $\mathbf{v}$ to the same temporal resolution as $\mathbf{d}_{\mathrm{MRI}}$, for details see Section 3. The objective is to find $(\mathbf{v}_{\mathrm{in}}, K)$ that minimizes this error functional $\mathcal{J}$. For more details on data assimilation see [8, 4, 17, 15, 2, 13].

To ensure that the optimization problem is well-posed, $\mathcal{J}$ is augmented with regularization terms $\mathcal{R}_1(\mathbf{v}_{\mathrm{in}})$ and $\mathcal{R}_2(K)$, which are designed to enforce the smoothness of the estimated boundary parameters $\mathbf{v}_{\mathrm{in}}$ and K. Specifically, we include regularization terms that penalize excessive spatial and temporal variations in the inlet velocity profile $\mathbf{v}_{\mathrm{in}}$ as well as spatial irregularities in the auxiliary slip parameter K. These regularization terms play a crucial role in stabilizing the optimization problem by preventing overfitting to noisy data and promoting physically realistic reconstructions of the boundary conditions.

With these regularization terms, the reduced error functional takes the form:

$$\begin{aligned}
\mathcal{J}_R(\mathbf{v}_{\mathrm{in}}, K) :&= \mathcal{J}(\mathbf{v}(\mathbf{v}_{\mathrm{in}}, K)) + \mathcal{R}_1(\mathbf{v}_{\mathrm{in}}) + \mathcal{R}_2(K) \\
&= \frac{1}{2TL^3}\|\mathcal{T}(\mathbf{v}(\mathbf{v}_{\mathrm{in}}, K)) - \mathbf{d}_{\mathrm{MRI}}\|^2_{L^2(0,T,L^2(\Omega))} \\
&\quad + \frac{\alpha}{2}\left(\frac{1}{TL^2}||\mathbf{v}_{\mathrm{in}}||^2_{L^2(0,T,L^2(\Gamma_{\mathrm{in}}))} + \frac{1}{T}||\nabla \mathbf{v}_{\mathrm{in}}||^2_{L^2(0,T,L^2(\Gamma_{\mathrm{in}}))} + \frac{T}{L^2}||\partial_t \mathbf{v}_{\mathrm{in}}||^2_{L^2(0,T,L^2(\Gamma_{\mathrm{in}}))}\right) \\
&\quad + \frac{\gamma}{2}||\nabla K||^2_{L^2(\Gamma_{\mathrm{in}})},
\end{aligned} \tag{4}$$

where T and L are the terminal time and the characteristic length, ensuring the terms have the same units. We conclude this section by summarizing the objective of our study:

$$\text{To find } (\mathbf{v}_{\mathrm{in}}, K) \text{ that minimizes } \mathcal{J}_R \text{ whereas } \mathbf{v}(\mathbf{v}_{\mathrm{in}}, K) \text{ solves (1).} \tag{5}$$

2 Segmentation and data preparation tools

In our computational experiments, preprocessing plays an essential role in constructing a computational mesh and an accompanying velocity field that accurately represent the underlying anatomy and flow dynamics. The preprocessing pipeline comprises two main stages: *segmentation* and *data preparation*. Initially, segmentation is employed to extract the region of interest from the original 3D steady-state free precession MRI (3D SSFP MRI) dataset, yielding the geometric description needed to generate the computational mesh. In the subsequent data preparation step, the velocity field extracted from the 4D phase-contrast MRI (4D PC-MRI) dataset is processed and interpolated onto the mesh. The assimilation procedure, as described in Section 1, is performed on both artificial data and real patient data.

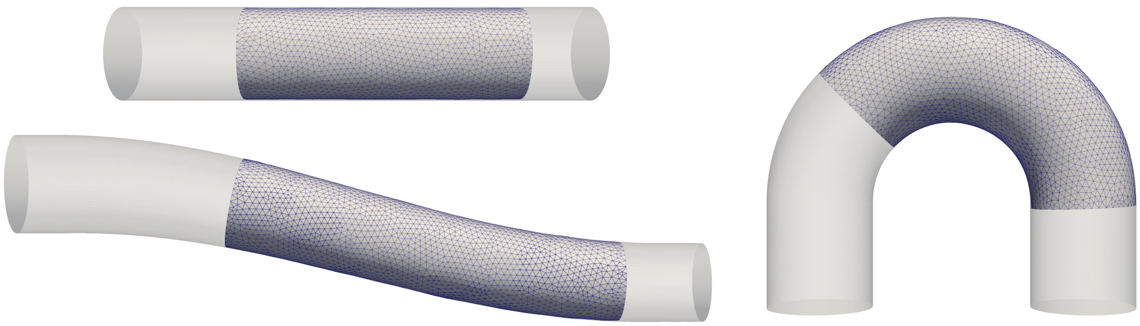

Figure 1: Shorter segments of the geometries used for the assimilation with edge length set to 1.5 mm.

2.1 Artificial data

In order to evaluate the capabilities of our approach, we first tested it using artificial data generated via a computational fluid dynamics (CFD) solver implemented in the finite element library Firedrake [7]. For these tests, reference velocity fields were generated for three distinct geometries representing segments of the thoracic aorta: (i) a straight tube with a constant radius; (ii) a slightly curved tube featuring a narrowing region with circular cross-sections; (iii) a tubular structure with a constant radius and a 180-degree bend that mimics the aortic arch, see Figure 1.

Generation of reference data The reference meshes were created using GMSH [6], setting the uniform edge length to 0.75 mm to achieve high resolution. The time discretization for the velocity field, represented in the weak form (7), employed a timestep $\Delta t = 0.01\,\mathrm{s}$. The reference velocity fields were generated for several values of $\kappa \in \{1, 4, 16, 200\}$ with an inlet velocity profile defined by

$$\mathbf{v}_{\mathrm{in}}(t, x, y) = V(t)\frac{4\mu R + 2\kappa(R^2 - (x^2 + y^2))}{4\mu R + \kappa R^2}, \tag{6}$$

where R is an inlet radius, x, y coordinates in the inlet plane and $V(t)$ is a periodic function with a period 0.8 s representing a simplified, though non-physiological, cardiac cycle for the purpose of code validation using synthetic data. The systolic phase lasts for 0.3 s and is represented by a parabolic profile with a peak velocity of 0.8 m/s, while the diastolic phase is modeled as a segment with constant zero velocity (see Figure 2). The velocity factor $V(t)$ mimics the flow generated by the left ventricle. This idealized inflow is chosen solely for validation purposes: its non-smooth transitions pose a greater challenge for numerical solvers. In simulations involving real patient data, the inflow velocity profile is obtained through data assimilation from MRI measurements. The CFD results computed with this high spatial and temporal resolution serve as the "ground truth" for the testing the assimilation method developed in this study.

Artificial mesh segmentation and post-processing of artificial data Since real MR images typically have lower spatial and temporal resolutions than CFD simulations, the "ground truth" velocity fields were post-processed to mimic MRI data quality. Figure 3 illustrates the complete post-processing workflow, including the resolution reduction and the addition of synthetic noise to mimic realistic acquisition artifacts.

Similarly to the process for real patient data (detailed in Section 2.2 below), the artificial computational meshes are generated via segmentation process. The high-resolution "ground truth" mesh is

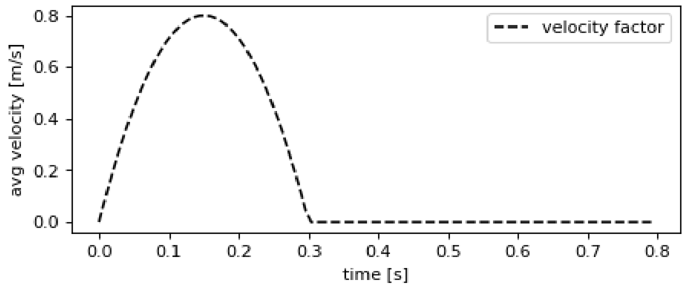

Figure 2: One period of a simplified inflow velocity factor $V(t)$.

embeded in a regular voxel grid (reflecting the resolution of 3D SSFP MRI) and voxels occupied by the by the "ground truth" mesh are marked. The obtained discontinous piecewise constant (DG0) marking function, which robustly captures the geometry, is then saved as a VTK file and segmented following the procedure described in Section 2.2, see the first line in Figure 3.

The second line in Figure 3 concerns downsampling of the velocity field. Temporal downsampling is performed by averaging the CFD velocity data over intervals defined by the MRI timestep $\Delta\tau$, which is set to 0.03 s, following the relation in (9). Subsequently, each time-averaged field is spatially resampled by projecting it onto a DG0 function space defined on a regular hexahedral grid with an edge length of 2.5 mm, matching the spatial resolution commonly found in MRI acquisitions.

2.2 Real patient data

After successfully verifying and validating our method on artificial data, we proceed to apply it to real datasets of seven healthy volunteers acquired at King's College London on 1.5 T Philips Achieva system [14]. Two types of MRI data are used: (i) 3D morphological MRI scan acquired during diastolic rest period (balanced steady state free precession; free breathing with using MRI breathing navigator; field of view $360 \times 360 \times 280\,\mathrm{mm}^3$; acquisition matrix $180 \times 177 \times 135$; voxel reconstructed to $\sim 1 \times 1 \times 1\,\mathrm{mm}^3$), which provides the anatomical structure necessary for generating the computational geometry; and (ii) a time-resolved 4D PC-MRI dataset capturing the full velocity field over the cardiac cycle in all three spatial directions (acquired in prospective ECG triggering during free breathing using MRI breathing navigator; acquired voxel size $\sim 2.3 \times 2.3 \times 2.3\,\mathrm{mm}^3$; temporal resolution ~ 35 ms; 8-fold accelerated acquisition reconstructed by k-t PCA technique [20] combined with a sparsifying transform [10]).

Segmentation and data reparation For real patient data, segmentation is performed using the open-source software 3D Slicer [9] with both manual intervention and the automated Total Segmentator tool [23], which is trained on 1,204 CT and 298 MR scans annotated by multiple researchers. The segmentation focuses on the region of interest extending from the left subclavian artery to the diaphragm. Figure 4 compares manual segmentation (green) with automatic segmentation (red) on a cross-section in the middle of the geometry.

Once segmented, a surface model is constructed using the Marching Cubes algorithm. The surface is then smoothed by applying the Taubin smoothing algorithm (30 iterations, $passband = 0.005$). Inlet and outlet boundaries are defined by clipping the geometry along the centerline, with 30% removed at the inlet and 10% at the outlet to ensure perpendicular boundary conditions relative to the centerline normal.

Further post-processing is performed with the Vascular Modeling Toolkit (VMTK) [1], which handles centerline extraction, additional surface smoothing, cutting, and scaling. The final geometry

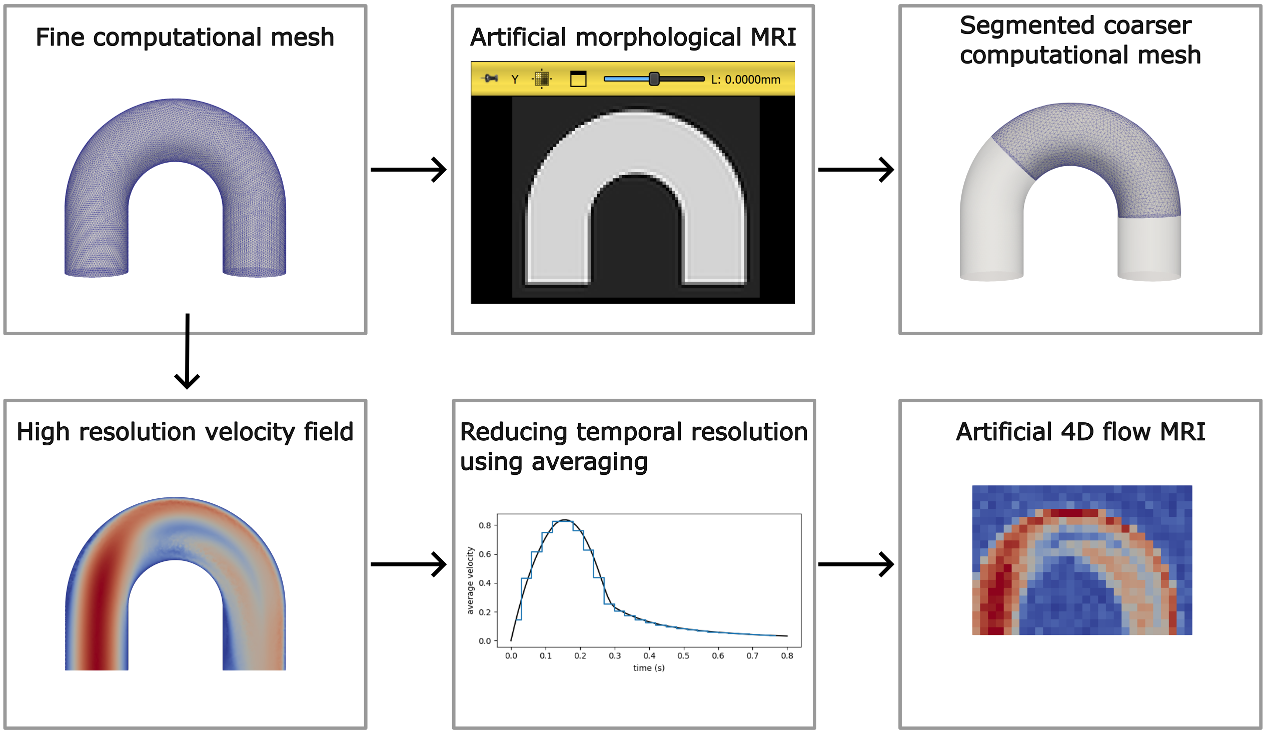

Figure 3: Workflow for generating artificial measurement data. The numerical simulation is performed on a fine computational mesh, the result is then downsampled in time and space and projected to a discontinuous piecewise constant finite element space.

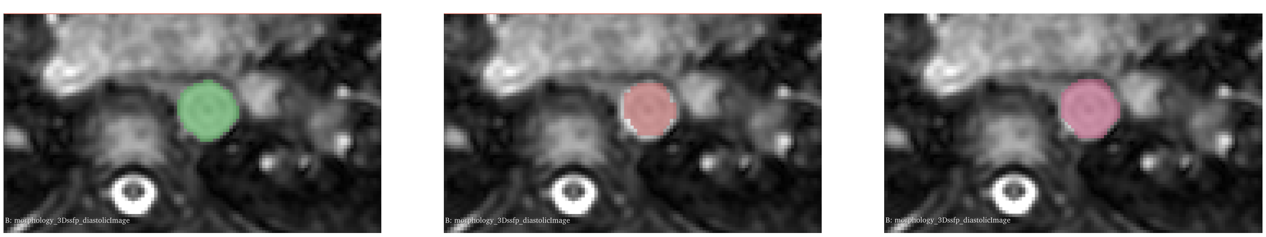

Figure 4: Comparison between the manual segmentation (left), automatic segmentation using Total Segmentator (middle) and automatic segmentation with an additional layer of pixels (right) on a cross-section in the middle of the geometry.

is scaled to meters, enclosed, and meshed using GMSH [6] with a uniform edge length of 1.5 mm for all simulations.

The velocity data from the 4D MRI were first converted to meters per second (m/s) and spatially aligned with the computational mesh through appropriate translation and rotation transformations. Originally defined on a regular grid as a continuous piecewise linear (CG1) function, the velocity field was then interpolated onto the computational mesh to ensure a consistent numerical representation suitable for the data assimilation process.

3 Numerical methods

As introduced in Section 1, the auxiliary slip parameter K and the inflow velocity profile $\mathbf{v}_{\text{in}}$ are identified via a data assimilation procedure. In this section, we describe the details of the assimilation procedure, of the discrete forward problem and of the specification of the measurement operator $\mathcal{T}$.

3.1 Assimilation procedure

The assimilation procedure aims to identify the optimal control variables $(K, \mathbf{v}_{\text{in}})$ by minimizing the cost functional $\mathcal{J}$ using the L-BFGS algorithm, a quasi-Newton method well suited for high-dimensional optimization. The gradients of $\mathcal{J}$ with respect to the control variables are efficiently and accurately computed via automatic differentiation provided by the Pyadjoint library [16].

Unlike the steady-state approach presented in [8], the present formulation performs assimilation over a full time period, capturing the transient dynamics of the flow. For further details regarding the structure and implementation of the assimilation framework, we refer the reader to [8].

3.2 Forward problem

We begin by discussing the numerical solution of the forward problem, i.e., the computation of the time-dependent velocity and pressure fields $\mathbf{v}, p$ given the auxiliary slip parameter K and a prescribed time-dependent inflow velocity profile $\mathbf{v}_{\text{in}}$.

To solve the time-dependent Navier–Stokes problem (1), we employ the finite element method (FEM) for spatial discretization in combination with the unconditionally stable implicit Euler method for time integration. The spatial discretization is closely related to that used in the steady case described in [8], with the principal difference being the inclusion of an additional term accounting for the time derivative.

Boundary conditions are imposed weakly using the non-symmetric Nitsche method with penalization [19]. The penalty parameter is denoted by $\beta_* > 0$, and $h > 0$ denotes the diameter of elements in the computational mesh. The weak formulation of the time-discrete problem reads as follows:

$$
\begin{aligned}
&\text{Find } \{(\mathbf{v}^i, p^i)\}_{i=1}^N \subset V_h \times P_h \text{ such that for all } (\phi, q) \in V_h \times P_h,\\
&\int_\Omega \frac{\rho}{\Delta t}(\mathbf{v}^i - \mathbf{v}^{i-1}) \cdot \phi \, \mathrm{d}x + \int_\Omega \rho(\nabla \mathbf{v}^i)\mathbf{v}^i \cdot \phi \, \mathrm{d}x + \int_\Omega \mathbb{T}(\mathbf{v}^i, p^i) \cdot \nabla\phi \, \mathrm{d}x + \int_\Omega q \operatorname{div} \mathbf{v}^i \, \mathrm{d}x\\
&- \int_{\partial\Omega_{\mathrm{in}}} \mathbb{T}(\mathbf{v}^i, p^i)\mathbf{n} \cdot \phi \, \mathrm{d}s + \int_{\partial\Omega_{\mathrm{in}}} (\mathbf{v}^i - \mathbf{v}^i_{\mathrm{in}}) \cdot \mathbb{T}(\phi, q)\mathbf{n} \, \mathrm{d}s + \frac{\beta_*\mu}{h} \int_{\partial\Omega_{\mathrm{in}}} (\mathbf{v}^i - \mathbf{v}^i_{\mathrm{in}}) \cdot \phi \, \mathrm{d}s\\
&+ \int_{\partial\Omega_{\mathrm{wall}}} \exp(K)\, \mathbf{v}^i_\tau \cdot \phi_\tau \, \mathrm{d}s - \int_{\partial\Omega_{\mathrm{wall}}} (\mathbb{T}(\mathbf{v}^i, p^i)\mathbf{n})_{\mathrm{n}} \cdot \phi_{\mathrm{n}} \, \mathrm{d}s + \int_{\partial\Omega_{\mathrm{wall}}} \mathbf{v}^i_{\mathrm{n}} \cdot (\mathbb{T}(\phi, q)\mathbf{n})_{\mathrm{n}} \, \mathrm{d}s\\
&+ \frac{\beta_*\mu}{h} \int_{\partial\Omega_{\mathrm{wall}}} \mathbf{v}^i_{\mathrm{n}} \cdot \phi_{\mathrm{n}} \, \mathrm{d}s - \int_{\partial\Omega_{\mathrm{out}}} \frac{1}{2}\rho(\mathbf{v}^i \cdot \mathbf{n})^2_-(\phi \cdot \mathbf{n}) \, \mathrm{d}s - \int_{\partial\Omega_{\mathrm{out}}} (\mathbb{T}(\mathbf{v}^i, p^i)\mathbf{n})_\tau \cdot \phi_\tau \, \mathrm{d}s\\
&+ \int_{\partial\Omega_{\mathrm{out}}} \mathbf{v}_\tau \cdot (\mathbb{T}(\phi, q)\mathbf{n})_\tau \, \mathrm{d}s + \frac{\beta_*\mu}{h} \int_{\partial\Omega_{\mathrm{out}}} \mathbf{v}^i_\tau \cdot \phi_\tau \, \mathrm{d}s = 0.
\end{aligned} \tag{7}
$$

The finite-dimensional spaces V_h and P_h are both chosen as piecewise linear (P1) elements to keep the computational cost manageable. Although this choice does not satisfy the inf-sup condition, it allows for efficient implementation, particularly in large-scale simulations. To compensate for the potential instability and to enhance the robustness of the discretization, we employ interior penalty (IP) stabilization [3]. This approach mitigates the effects of discontinuities and sharp gradients across element interfaces, thereby ensuring stable and accurate numerical solutions. The stabilization terms added to (7) are:

$$
\begin{aligned}
\alpha_v \sum_{K \in \mathcal{F}} \int_K \rho h^2 [\nabla \mathbf{v}] \cdot [\nabla \phi] \, \mathrm{d}s + \alpha_i \sum_{K \in \mathcal{F}} \int_K \rho h^2 (\mathbf{v} \cdot \mathbf{n}) [\nabla \mathbf{v}] \cdot [\nabla \phi] \, \mathrm{d}s&\\
+ \alpha_p \sum_{K \in \mathcal{F}} \int_K \frac{h^2}{\rho} [\nabla p] \cdot [\nabla q] \, \mathrm{d}s,&
\end{aligned} \tag{8}
$$

where $\mathcal{F}$ is the set of interior mesh faces, and $[\cdot]$ denotes the jump of a quantity across a face.

The problem is implemented using the Firedrake finite element framework [7]. Nonlinearities are handled using the full Newton method, and the resulting linear systems are solved with the direct solver MUMPS.

3.3 Measurement operator

As discussed in Section 1, a measurement operator $\mathcal{T}$ is used to compare the simulated velocity field with experimental MRI data sampled at discrete time steps.

The operator $\mathcal{T}_{\mathrm{avg}}$ is constructed based on the understanding that each MRI measurement reflects an average over a small time interval. Specifically, it computes the mean velocity over a time window I_i centered at each MRI sampling time $t_{\mathrm{MRI},i}$:

$$
\mathcal{T}_{\mathrm{avg}}(\mathbf{v})(t_{\mathrm{MRI},i}) = \frac{1}{n_i} \sum_{t_j \in I_i} \mathbf{v}(t_j), \quad I_i = \left[t_{\mathrm{MRI},i} - \frac{1}{2}\Delta_{\mathrm{MRI}},\, t_{\mathrm{MRI},i} + \frac{1}{2}\Delta_{\mathrm{MRI}} \right], \tag{9}
$$

where n_i is the number of simulation time steps contained in I_i, and Δ_{MRI} is the time resolution of the MRI measurements.

The operator $\mathcal{T}_{\mathrm{avg}}$ ensures that the computed and measured velocities are temporally aligned, allowing for meaningful comparison and efficient assimilation.

4 Tests and results

We perform numerical experiments on both artificial and patient-specific datasets. The physical and numerical parameters used in solving the forward problem are summarized in Table 1.

All simulations are initialized at $t_0 = -0.02\,\mathrm{s}$, corresponding to two time steps prior to the interval of interest $(0, T)$. This early initialization helps suppress transient pressure spikes that typically arise from the abrupt activation of boundary conditions at the start of the simulation.

To reduce computational cost, the simulations are limited to a single cardiac cycle rather than multiple periods. Since t_0 precedes the onset of systole and lies outside the inference window, we initialize the velocity field as $\mathbf{v}(t_0) = \mathbf{v}_0 = \mathbf{0}$ without changing the solution on the interval $(0, T)$.

Symbol	Name	Value	Unit
μ	dynamic viscosity	3.8955×10^{-3}	$\mathrm{kg \cdot m^{-1} s^{-1}}$
ρ	density	1,050	$\mathrm{kg \cdot m^{-1}}$
Δt	simulation timestep	0.01	s
t_0	initial time	-0.02	s
T	terminal time	≈ 0.8	s
L	characteristic length	0.01	m
γ_*	-	0.25	$\mathrm{m^2 \cdot s \cdot kg^{-1}}$
β_*	Nitsche penalty parameter	1,000	-
α_v	stabilization weight	5.00×10^{-4}	-
α_i	stabilization weight	1.00×10^{-2}	-
α_p	stabilization weight	1.0	-
h	computational mesh size	1.50×10^{-3}	m
Δ_{MRI}	MRI time step	$29 - 36$	ms

Table 1: Parameters used to solve the forward problem.

4.1 Numerical experiments with artificial data

We use three different artificial domains (see Figure 1). Artificial data are generated for a range of slip parameter values $\kappa \in \{1, 4, 16, 200\}$. The value $\kappa = 200$ is chosen in such a way that it approximates no-slip: as for $\kappa = 200$ the resultant slip length is in the range of erythrocyte diameter, below this level blood cannot be reasonably modeled as a continuum.

The recovered optimal slip parameter κ_{opt}, along with the values of the functionals $\mathcal{J}_R$, are presented in Tables 2–4. The dependence of the optimal slip parameter κ_{opt} on mesh resolution is provided in Tables 5–7.

The results indicate that when the true boundary condition is no-slip ($\kappa = 200$), the recovered slip parameter κ_{opt} exceeds 20. With mesh refinement, κ_{opt} increases to 34 for the straight tube and exceeds 60 for the more realistic bent and arch tubes, as shown in Tables 5–7. These findings suggest that values of κ_{opt} below 20 do not represent a no-slip condition.

4.2 Numerical results with patient-specific data

We use seven different sets of MRI data for the descending thoracic aorta, as described in Section 2.2. The slip parameter, obtained through our fitting process, is highly sensitive to the domain used for data fitting. If the segmented domain is smaller than the actual lumen, velocities located closer

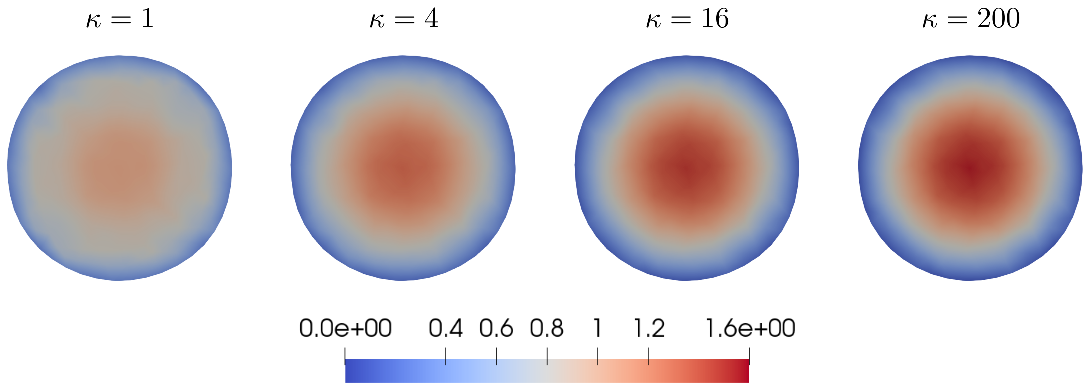

Figure 5: Velocity inflow for different slip parameters κ in a straight tube.

"ground truth" κ	1	4	16	200
κ_{opt}	6.27	8.44	15.23	23.83
$\mathcal{J}_R$	1.54×10^{-2}	1.71×10^{-2}	1.83×10^{-2}	2.14×10^{-2}

Table 2: Optimal slip parameter κ and functional $\mathcal{J}_R$ for artificial straight tube.

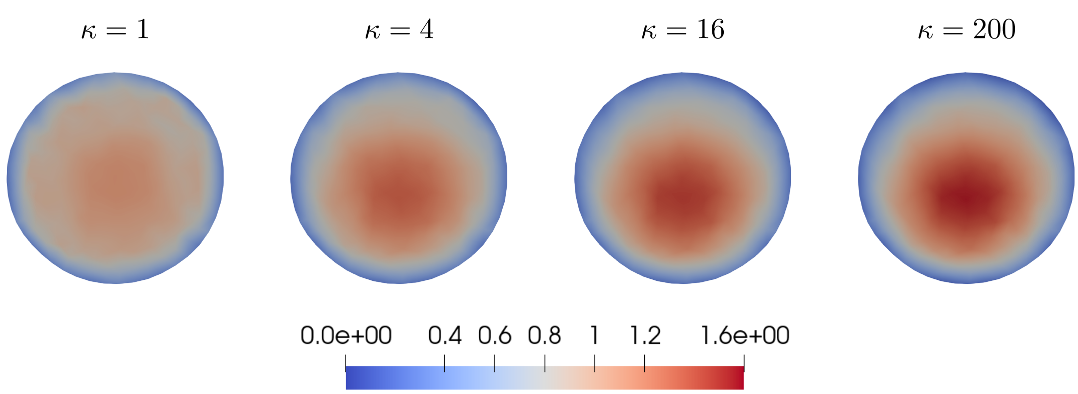

Figure 6: Velocity inflow for different slip parameters κ in a bent tube.

"ground truth" κ	1	4	16	200
κ_{opt}	7.28	8.56	15.67	28.60
$\mathcal{J}_R$	2.63×10^{-2}	3.22×10^{-2}	3.54×10^{-2}	4.04×10^{-2}

Table 3: Optimal slip parameter κ and functional $\mathcal{J}_R$ for artificial bent tube.

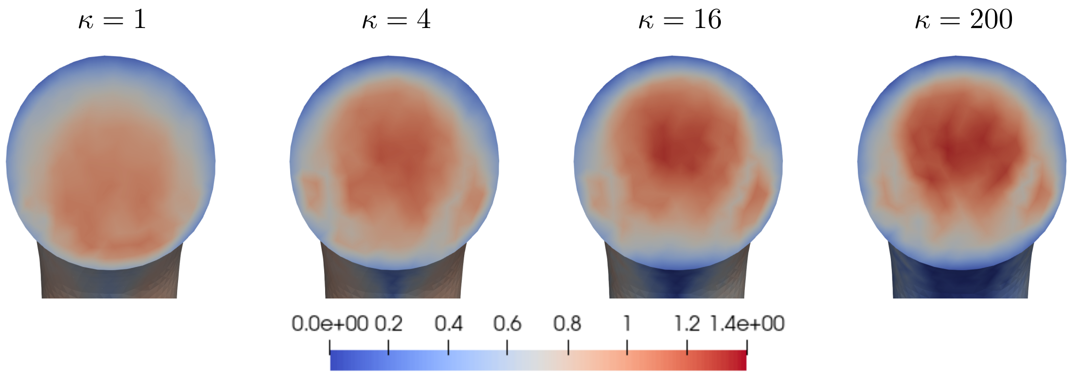

Figure 7: Velocity inflow for different slip parameters κ in an arch tube.

"ground truth" κ	1	4	16	200
κ_{opt}	2.66	4.82	12.70	58.23
$\mathcal{J}_R$	4.59×10^{-2}	6.09×10^{-2}	6.74×10^{-2}	1.32×10^{-1}

Table 4: Optimal slip parameter κ and functional for artificial arch tube.

"ground truth" κ	1	4	16	200
resolution 2.5 mm	6.28	8.70	15.39	22.02
resolution 1.25 mm	4.04	6.65	14.68	28.91
resolution 0.625 mm	2.49	5.20	14.59	34.09

Table 5: Resolution comparison for a straight tube.

"ground truth" κ	1	4	16	200
resolution 2.5 mm	7.18	8.73	15.45	26.54
resolution 1.25 mm	6.71	9.15	19.84	44.19
resolution 0.625 mm	6.11	9.30	22.60	72.13

Table 6: Resolution comparison for a bent tube.

"ground truth" κ	1	4	16	200
resolution 2.5 mm	2.11	4.69	11.93	34.71
resolution 1.25 mm	1.91	4.53	14.44	52.16
resolution 0.625 mm	1.91	4.79	13.62	60.44

Table 7: Resolution comparison for an arch tube.

to the center are incorrectly interpreted as boundary velocities, leading to an underestimated slip parameter κ. Conversely, if the domain extends beyond the true lumen, near-zero velocities outside the vessel may be misclassified as boundary data, resulting in an overestimated value of κ. Accurate lumen segmentation is therefore essential for a reliable estimation of the slip parameter.

We segment the lumen using two methods: (i) manual segmentation of the MRI data and (ii) automatic segmentation using artificial intelligence, as implemented in TotalSegmentator [23]. The primary advantage of the automatic method is its consistency and reproducibility. Unlike manual segmentation, it removes operator bias and ensures objective results. Figure 4 compares the manual and automatic segmentation approaches. Notably, the domain obtained from automatic segmentation is slightly smaller than that from manual segmentation, which in turn leads to a lower fitted slip parameter κ.

To account for this discrepancy, we also performed fitting using the domain generated by TotalSegmentator, expanded by one additional pixel layer (with $1\,\text{px} = 1.05\,\text{mm}$ in our MRI data). Adding this extra layer increases the fitted slip parameter κ, effectively bringing the model closer to the no-slip condition. If, even in this expanded setting, a significant degree of slip is still observed, it further strengthens the robustness and relevance of the results.

For all seven datasets, we apply our fitting methodology and present the results in Figures 8–13, comparing the velocity field for no-slip boundary condition with two slip models: one employing a constant, optimally fitted slip parameter κ_{opt}, and the other using a spatially varying slip parameter $\kappa_{\text{opt}}(x)$. The rightmost panel of each figure shows the spatial distribution of the slip parameter, providing insight into how wall interaction varies across the domain.

Interestingly, across all seven datasets, the velocity profiles produced by the constant and spatially varying slip models are remarkably similar. However, the spatial distribution of the slip parameter κ varies significantly. Along most of the wall, κ remains close to zero, indicating nearly perfect slip conditions. In contrast, in localized regions, κ becomes very large, effectively imposing a no-slip condition. This suggests that only a small part of the boundary significantly resists the flow.

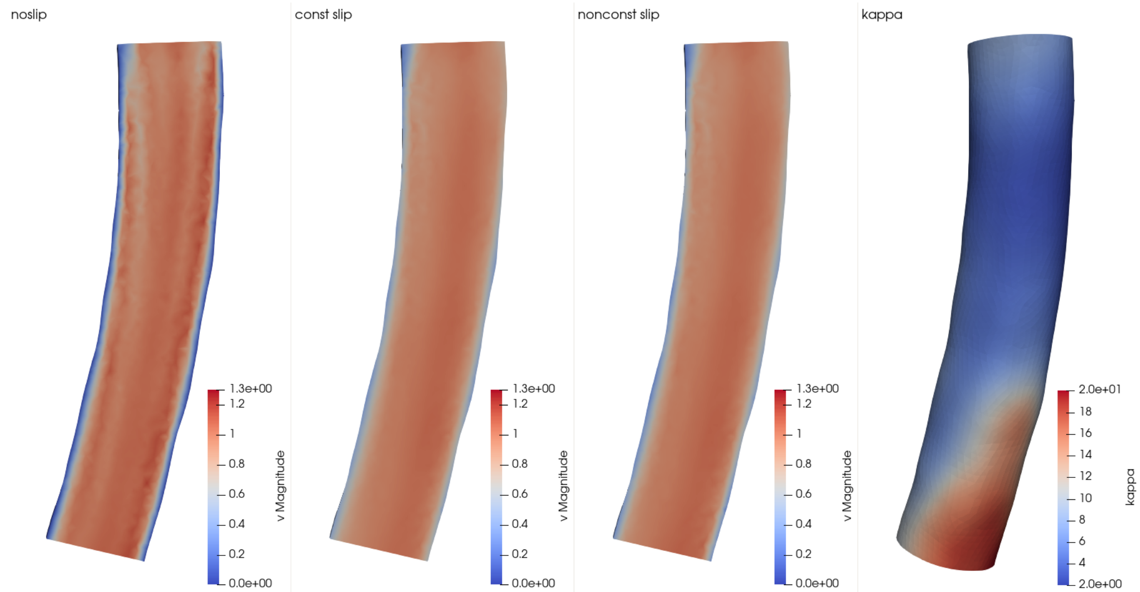

Figure 8: Dataset 1 (left to right): velocity profile for no-slip; velocity profile for optimally fitted constant slip parameter κ_{opt}; velocity profile for fitted space varying slip parameter $\kappa_{\text{opt}}(x)$; spatial distribution of the slip function $\kappa_{\text{opt}}(x)$.

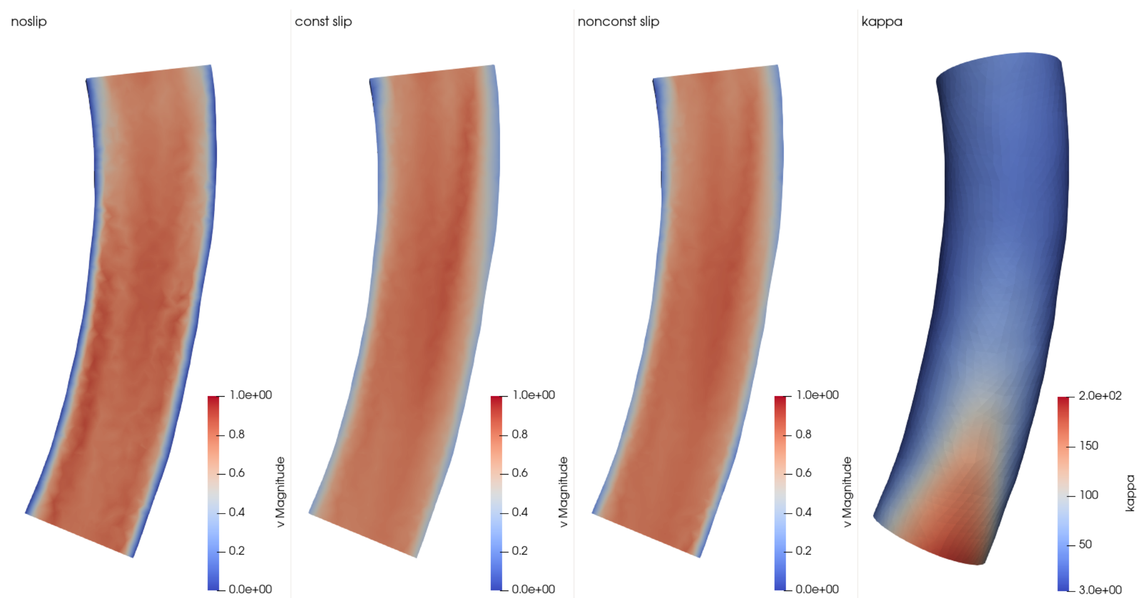

Figure 9: Dataset 2 (left to right): velocity profile for no-slip; velocity profile for optimally fitted constant slip parameter κ_{opt}; velocity profile for fitted space varying slip parameter $\kappa_{\text{opt}}(x)$; spatial distribution of the slip function $\kappa_{\text{opt}}(x)$.

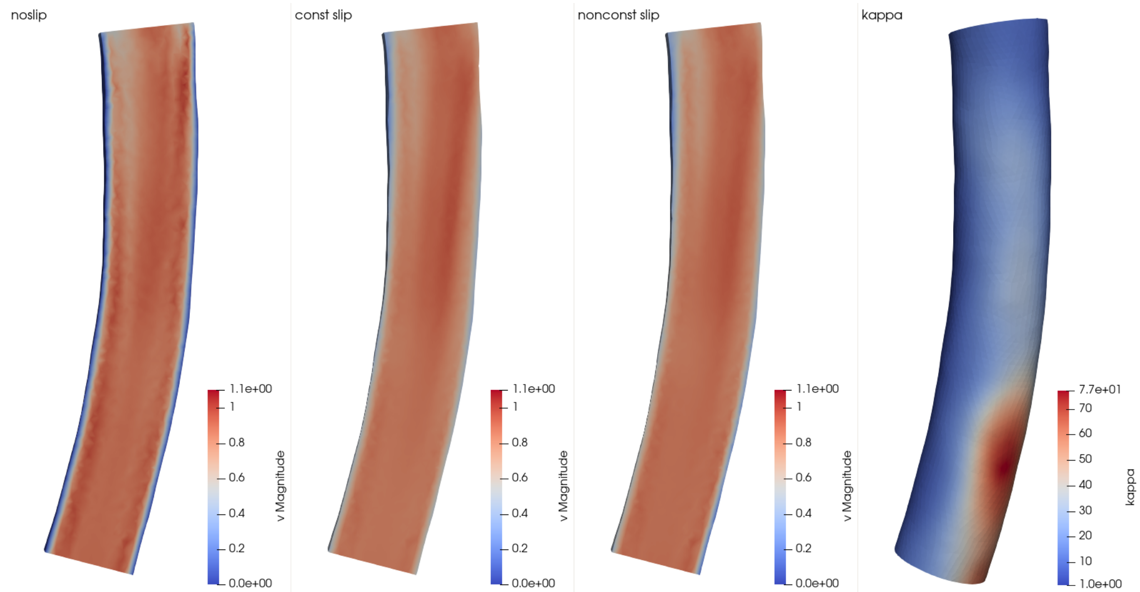

Figure 10: Dataset 3 (left to right): velocity profile for no-slip; velocity profile for optimally fitted constant slip parameter κ_{opt}; velocity profile for fitted space varying slip parameter $\kappa_{\text{opt}}(x)$; spatial distribution of the slip function $\kappa_{\text{opt}}(x)$.

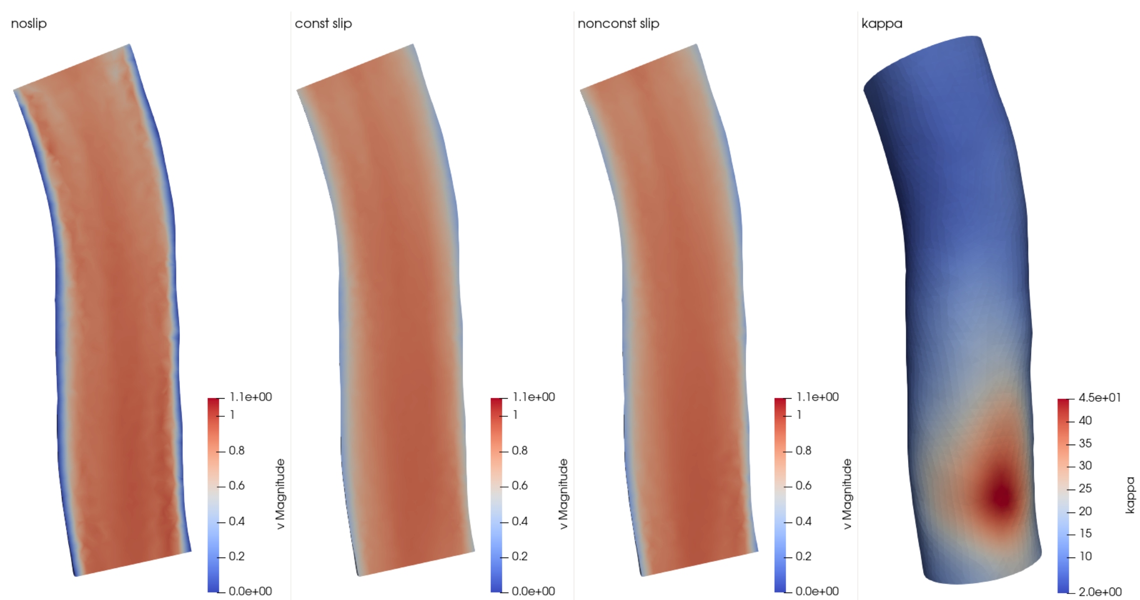

Figure 11: Dataset 4 (left to right): velocity profile for no-slip; velocity profile for optimally fitted constant slip parameter κ_{opt}; velocity profile for fitted space varying slip parameter $\kappa_{\text{opt}}(x)$; spatial distribution of the slip function $\kappa_{\text{opt}}(x)$.

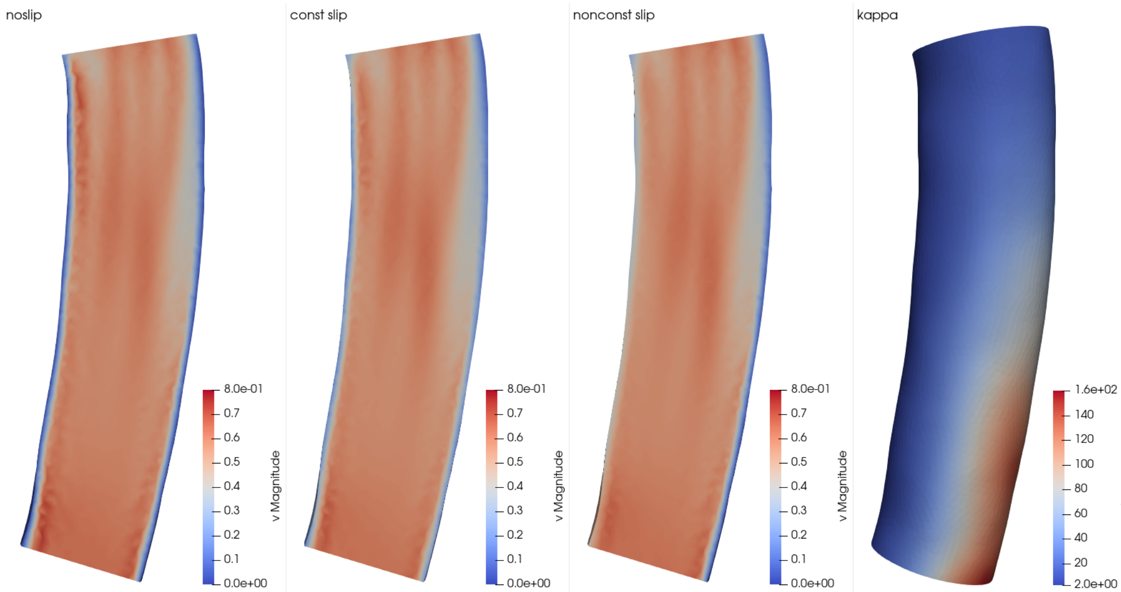

Figure 12: Dataset 5 (left to right): velocity profile for no-slip; velocity profile for optimally fitted constant slip parameter κ_{opt}; velocity profile for fitted space varying slip parameter $\kappa_{\mathrm{opt}}(x)$; spatial distribution of the slip function $\kappa_{\mathrm{opt}}(x)$.

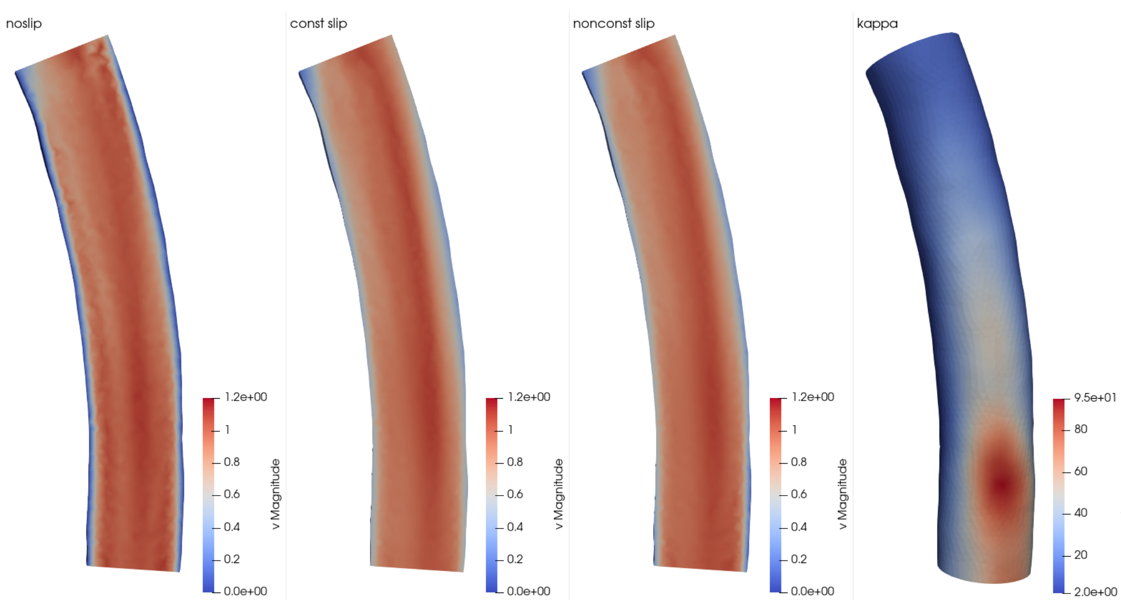

Figure 13: Dataset 6 (left to right): velocity profile for no-slip; velocity profile for optimally fitted constant slip parameter κ_{opt}; velocity profile for fitted space varying slip parameter $\kappa_{\mathrm{opt}}(x)$; spatial distribution of the slip function $\kappa_{\mathrm{opt}}(x)$.

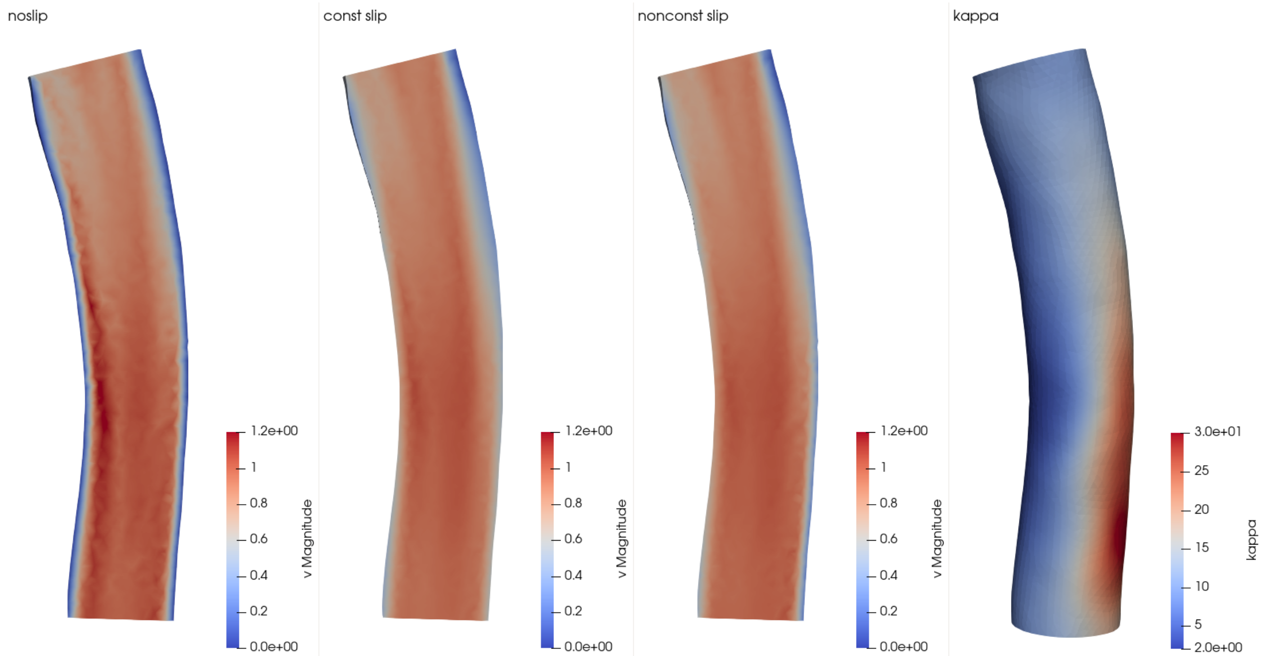

Figure 14: Dataset 7 (left to right): velocity profile for no-slip; velocity profile for optimally fitted constant slip parameter κ_{opt}; velocity profile for fitted space varying slip parameter $\kappa_{\text{opt}}(x)$; spatial distribution of the slip function $\kappa_{\text{opt}}(x)$.

For each segmentation method (manual, automatic, and automatic with one additional pixel layer), Figure 15 shows the time evolution of the average tangential velocity along the wall, as well as the average velocity over the entire domain, for all seven segmented datasets. The average tangential velocity on the vessel wall Γ_{wall} and average velocity over the whole domain Ω are defined as

$$v_{\text{avg}}^{\Gamma_{\text{wall}}}(t) = \frac{1}{|\Gamma_{\text{wall}}|}\int_{\Gamma_{\text{wall}}} |\mathbf{v}_\tau| \,\mathrm{d}S, \tag{10}$$

$$v_{\text{avg}}^{\Omega}(t) = \frac{1}{|\Omega|}\int_{\Omega} |\mathbf{v}| \,\mathrm{d}x. \tag{11}$$

Under the classical no-slip boundary condition, the quantity $v_{\text{avg}}^{\Gamma_{\text{wall}}}$ would be identically zero. In contrast, our results consistently show values ranging from 30% to 60% of the average velocity over the domain, indicating a pronounced degree of slip at the wall.

The percentages shown below each graph represent the ratio of the space-time averaged tangential wall velocity to the space-time averaged velocity over the entire domain:

$$R = \frac{\displaystyle\int_0^T v_{\text{avg}}^{\Gamma_{\text{wall}}}(t)\,\mathrm{d}t}{\displaystyle\int_0^T v_{\text{avg}}^{\Omega}(t)\,\mathrm{d}t}. \tag{12}$$

This ratio provides a compact and robust quantification of slip intensity over the cardiac cycle.

The optimal slip parameters κ_{opt} for each MRI dataset and segmentation method are summarized in Table 8. The corresponding slip lengths, computed as $\beta = \mu/\kappa_{\text{opt}}$, are reported in Table 9, while average tangential wall velocities during systole $v_{\text{avg,sys}}$ are provided in Table 10.

Dataset	D1	D2	D3	D4	D5	D6	D7
Manual segmentation	3.89	5.42	5.29	4.96	18.26	5.35	4.59
Automatic segmentation	1.62	3.09	2.14	1.49	4.40	2.49	2.22
Automatic segmentation with an additional layer	4.60	8.91	5.81	4.28	16.29	7.93	13.32

Table 8: Fitted slip parameters κ [Pa s m^{-1}] for different MRI datasets and different segmentation methods.

Dataset	D1	D2	D3	D4	D5	D6	D7
Manual segmentation	1.0	0.72	0.74	0.79	0.21	0.73	0.85
Automatic segmentation	2.41	1.26	1.82	2.61	0.89	1.56	1.76
Automatic segmentation with an additional layer	0.85	0.44	0.67	0.91	0.24	0.49	0.29

Table 9: Slip length $\beta = \mu/\kappa$ [mm] corresponding to fitted slip parameters κ.

Notably, automatic segmentation tends to yield lower values of κ_{opt} than manual segmentation, which corresponds to higher average tangential wall velocities. This is consistent with the slightly smaller segmented domains obtained through the automatic method, as discussed previously. Across all datasets, the recovered slip parameters remain well below 20 for automatic segmentation with one additional layer of pixels; for five of seven datasets, the value of slip parameter κ is below 10. Since larger values of κ imply reduced slip—with the no-slip limit corresponding to $\kappa \to \infty$—and given that the observed wall velocities are consistently nonzero, these results provide compelling evidence that the classical no-slip condition does not hold *in vivo*.

Dataset	D1	D2	D3	D4	D5	D6	D7
Manual segmentation	0.53	0.36	0.48	0.45	0.16	0.50	0.52
Automatic segmentation	0.74	0.51	0.66	0.63	0.37	0.67	0.67
Automatic segmentation with an additional layer	0.53	0.30	0.46	0.47	0.17	0.42	0.34

Table 10: Fitted average tangential velocities in systole $v_{\text{avg,sys}}$ [m/s] for different MRI datasets and different segmentation methods. The methods include manual segmentation, automatic segmentation using the TotalSegmentator tool, and automatic segmentation with an expanded domain by adding one additional layer of pixels (1 px = 1.05 mm in the MRI data).

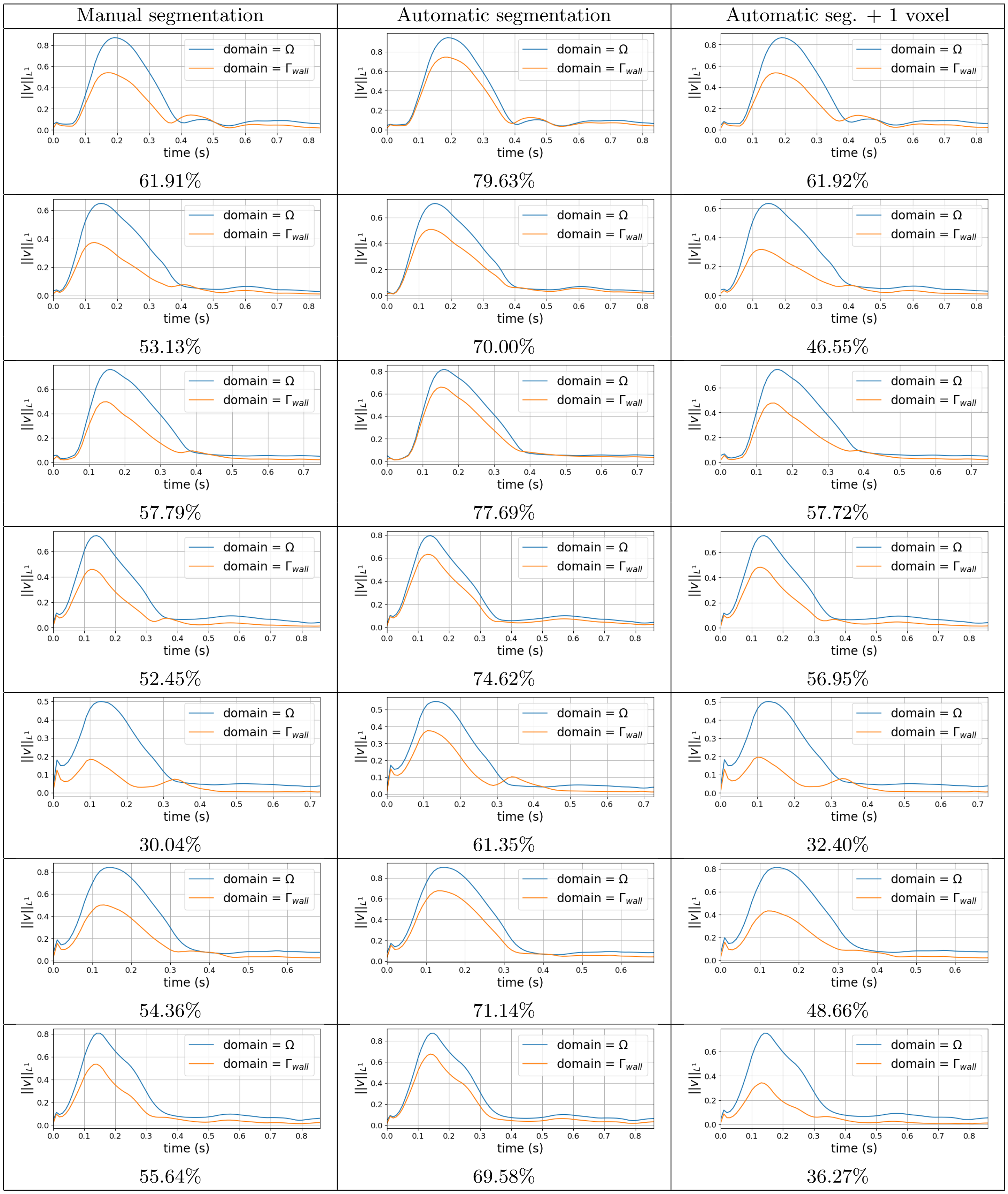

Figure 15: Time evolution of the average tangential velocity along the wall $v_{\text{avg}}^{\Gamma_{\text{wall}}}(t)$ and the average velocity over the entire domain $v_{\text{avg}}^{\Omega}(t)$, for seven datasets using manual segmentation (*left column*), automatic segmentation (*middle column*) and automatic segmentation with one additional voxel layer (*right column*).

References

[1] L. Antiga, M. Piccinelli, L. Botti, B. Ene-Iordache, A. Remuzzi, and D. A. Steinman. “An image-based modeling framework for patient-specific computational hemodynamics”. In: *Medical & Biological Engineering & Computing* 46.11 (2008), pp. 1097–1112. DOI: 10.1007/s11517-008-0420-1.

[2] R. Aróstica, C. Bertoglio, and D. Nolte. “Parameter Estimation in Cardiac Fluid–Structure Interaction from Fluid and Solid Measurements”. In: *International Conference on Functional Imaging and Modeling of the Heart*. Springer. 2025, pp. 378–389.

[3] E. Burman. “Interior penalty variational multiscale method for the incompressible Navier–Stokes equation: Monitoring artificial dissipation”. In: *Computer Methods in Applied Mechanics and Engineering* 196.41-44 (2007), pp. 4045–4058. DOI: 10.1016/j.cma.2007.03.025.

[4] D. Chapelle, M. Fragu, V. Mallet, and P. Moireau. “Fundamental principles of data assimilation underlying the Verdandi library: applications to biophysical model personalization within euHeart”. In: *Medical & Biological Engineering & Computing* 51 (2013), pp. 1221–1233.

[5] V. S. J. Craig, C. Neto, and D. R. M. Williams. “Shear-Dependent Boundary Slip in an Aqueous Newtonian Liquid”. In: *Physical Review Letters* 87.5 (July 2001). DOI: 10.1103/physrevlett.87.054504.

[6] C. Geuzaine and J.-F. Remacle. “Gmsh: A 3-D finite element mesh generator with built-in pre- and post-processing facilities”. In: *International Journal for Numerical Methods in Engineering* 79.11 (May 2009), pp. 1309–1331. DOI: 10.1002/nme.2579.

[7] D. A. Ham et al. *Firedrake User Manual*. First edition. Imperial College London et al. May 2023. DOI: 10.25561/104839.

[8] A. Jarolímová and J. Hron. “Determination of Navier’s slip parameter using data assimilation”. In: *Applied Mathematics and Computation* 489 (2025), p. 129157. DOI: https://doi.org/10.1016/j.amc.2024.129157.

[9] R. Kikinis, S. D. Pieper, and K. G. Vosburgh. “3D Slicer: A Platform for Subject-Specific Image Analysis, Visualization, and Clinical Support”. In: *Intraoperative Imaging and Image-Guided Therapy*. Springer New York, Nov. 2013, pp. 277–289. DOI: 10.1007/978-1-4614-7657-3_19.

[10] V. Knobloch, P. Boesiger, and S. Kozerke. “Sparsity transform k-t principal component analysis for accelerating cine three-dimensional flow measurements”. In: *Magn Reson Med* 70.1 (2013), pp. 53–63. DOI: 10.1002/mrm.24431.

[11] J. Málek and K. R. Rajagopal. “On a methodology to determine whether the fluid slips adjacent to a solid surface”. In: *International Journal of Non-Linear Mechanics* 157 (2023). DOI: 10.1016/j.ijnonlinmec.2023.104512.

[12] J. Málek and K. R. Rajagopal. “On determining Navier’s slip parameter at a solid boundary in flows of a Navier–Stokes fluid”. In: *Physics of Fluids* 36.1 (2024). DOI: 10.1063/5.0185585.

[13] J. Manganotti, F. Caforio, F. Kimmig, P. Moireau, and S. Imperiale. “Coupling reduced-order blood flow and cardiac models through energy-consistent strategies: modeling and discretization”. In: *Advanced Modeling and Simulation in Engineering Sciences* 8.1 (2021), p. 21.

[14] D. Marlevi et al. “Altered Aortic Hemodynamics and Relative Pressure in Patients with Dilated Cardiomyopathy”. In: *Journal of Cardiovascular Translational Research* 15.4 (Dec. 2021), pp. 692–707. DOI: 10.1007/s12265-021-10181-1.

[15] A. L. Marsden. “Optimization in cardiovascular modeling”. In: *Annual review of fluid mechanics* 46.1 (2014), pp. 519–546.

[16] S. Mitusch, S. Funke, and J. Dokken. “dolfin-adjoint 2018.1: automated adjoints for FEniCS and Firedrake”. In: *Journal of Open Source Software* 4.38 (2019), p. 1292. DOI: 10.21105/joss.01292.

[17] P. Moireau, C. Bertoglio, N. Xiao, C. A. Figueroa, C. Taylor, D. Chapelle, and J.-F. Gerbeau. “Sequential identification of boundary support parameters in a fluid-structure vascular model using patient image data”. In: *Biomechanics and modeling in mechanobiology* 12 (2013), pp. 475–496.

[18] C. Neto, D. R. Evans, E. Bonaccurso, H.-J. Butt, and V. S. J. Craig. “Boundary slip in Newtonian liquids: a review of experimental studies”. In: *Reports on Progress in Physics* 68.12 (Oct. 2005), pp. 2859–2897. DOI: 10.1088/0034-4885/68/12/r05.

[19] J. Nitsche. “Über ein Variationsprinzip zur Lösung von Dirichlet-Problemen bei Verwendung von Teilräumen, die keinen Randbedingungen unterworfen sind”. In: *Abhandlungen aus dem mathematischen Seminar der Universität Hamburg*. Vol. 36. 1. Springer. 1971, pp. 9–15.

[20] H. Pedersen, S. Kozerke, S. Ringgaard, K. Nehrke, and W. Kim. “k-t PCA: Temporally constrained k-t BLAST reconstruction using principal component analysis”. In: *Magn Reson Med* 62 (2009), pp. 706–716.

[21] D. Scarselli, J. M. Lopez, A. Varshney, and B. Hof. “Turbulence suppression by cardiac-cycle-inspired driving of pipe flow”. In: *Nature* 621.7977 (Sept. 2023), pp. 71–74. DOI: 10.1038/s41586-023-06399-5.

[22] O. I. Vinogradova and G. E. Yakubov. “Surface roughness and hydrodynamic boundary conditions”. In: *Physical Review E* 73.4 (Apr. 2006). DOI: 10.1103/physreve.73.045302.

[23] J. Wasserthal et al. “TotalSegmentator: Robust Segmentation of 104 Anatomic Structures in CT Images”. In: *Radiology: Artificial Intelligence* 5.5 (2023), e230024. DOI: 10.1148/ryai.230024.